Supporting Information

Elucidating the role of heteroatoms in hypercrosslinked polymer adsorbents for atmospheric water harvesting

Paul Schweng,[a,b] Lisa Pammer,[a] Robert T. Woodward[a]*

[a] Institute of Materials Chemistry and Research, Faculty of Chemistry, University of Vienna, Währinger Straße 42, 1090, Vienna, Austria

[b] Vienna Doctoral School in Chemistry, University of Vienna, Währinger Straße 42, 1090, Vienna, Austria

*Corresponding author:

E-mail: robert.woodward@univie.ac.at

Section 1

Experimental methods

1.1. Materials

All chemicals were obtained from commercial sources and used without further purification. Fluorene (98%), carbazole (synthesis grade), dibenzofuran (synthesis grade), dibenzothiophene (98%), dibenzothiophenone sulfone (97%), 4,4‘-bis(chloromethyl)-1,1‘-biphenyl (95%), $FeCl_3$ (reagent grade, 97%) and 1,2-dichloroethane (ACS reagent, ≥99%), were purchased from Sigma-Aldrich. Methanol (≥99.8%) was purchased from Fisher Scientific.

1.2. Characterisation of hypercrosslinked polymers

Fourier-transform infrared spectroscopy (FTIR) measurements were carried out using a Tensor II FTIR spectrometer (Bruker) with a Bruker Optics Platinum ATR module. Measurements were performed on finely ground samples in ambient conditions. Spectra were recorded in the 400–4000 cm^{-1} range in a double-sided forward-backward acquisition mode with a spectral resolution of 4 cm^{-1}. The instrument was purged with dry air during measurement, and spectra were obtained by averaging 32 scans and were calculated using a Blackman–Harris 3-term apodisation function and a zero-filling factor of 4. Spectra were recorded and analysed using the OPUS 7.5 software.

Solid-state NMR was carried out on a Bruker Avance NEO 500 wide bore system (Bruker BioSpin) using a 4 mm triple resonance magic angle spinning probe. Between 15–25 mg of material was packed into a 4 mm zirconia CRAMPS rotor. The resonance frequency for ^{13}C NMR was 125.78 MHz and the MAS rotor spinning was set to 14 kHz. Cross-polarisation was achieved by a ramped contact pulse with a contact time of 3 ms. During acquisition, ^{1}H was high power decoupled using SPINAL with 64 phase permutations. The ^{1}H $\pi/2$ pulse was 2.5 μs, the relaxation delay was set to 4 s, and with roughly 2000 scans a sufficient signal-to-noise was achieved. The chemical shifts for ^{13}C are reported in ppm and are referenced externally to adamantane by setting the low field signal to 38.48 ppm.

X-ray photoelectron spectroscopy (XPS) was performed on a Nexsa Photoelectron Spectrometer (Thermo Scientific). High-resolution spectra of carbon (C 1s 279–298 eV), nitrogen (N 1s 394–410 eV), oxygen (O 1s 525–545 eV), and sulphur (S 2p 160–174 eV) were recorded with a resolution of 0.1 eV and a pass energy of 50 eV. All measurements were performed using Al-Kα X-rays with a spot size of 400 µm. Evaluation of the spectra was performed using Avantage software (v5.9931, Thermo Fisher Scientific) and the atomic composition of the sample was determined from the peak area using the scaling factor database ALTHERMO1. The data were averaged over three measurements.

Elemental analysis was carried out using an EA 3000 CHNS-O analyser (Eurovector). For each run, 0.75–3.0 mg of sample was weighed into 4 × 6 mm tin vials using a microbalance (Sartorius ME 5 OCE). Samples were analysed in triplicate. The combustion and reduction temperatures were set to 1000 °C (1480 °C for oxygen analysis) and 750 °C, respectively, with high-purity helium (99.999+) as the carrier gas.

Thermogravimetric analysis was performed using a Discovery TGA (TA instruments). Approximately 10 mg of sample was heated from room temperature to 800 °C at a rate of 10 $°C \cdot min^{-1}$ under dry air flow of 100 $mL \cdot min^{-1}$.

N_2 isotherms were recorded at −196 °C using a 3Flex (Micromeritics) or, for repeat measurements, a TriStar II (Micromeritics). Prior to analysis, 50–100 mg of sample was degassed under N_2 flow at 120 °C for 14 h using a FlowPrep 060 (Micromeritics). Specific surface areas (SSA_{BET}) were determined via the Brunauer–Emmett–Teller (BET) method in the relative pressure range $P/P_0 = 0.05$–0.2. Pore size distributions (PSDs) were derived from the adsorption branch using quenched solid density functional theory (QSDFT) with a carbon slit/cylindrical pore model. The total pore volume (V_{tot}), micropore volume (V_{mic}), and mesopore volume (V_{mes}) were obtained from cumulative QSDFT pore volume distributions. For V_{tot}, data points at $P/P_0 > 0.97$ were excluded to avoid contributions from bulk N_2 condensation.

1.3. Water sorption experiments

Dynamic vapour sorption (DVS) experiments were carried out on a DVS-Resolution (Surface Measurement Systems) using ~10 mg of sample loaded into a quartz crystal pan. Measurements started at 0% RH to remove residual water, followed by stepwise increases up to 90% RH in 10% increments. Deionised water was used to generate the desired RH. Each step was equilibrated for 5 h before measurement. Experiments were performed at 25 °C unless stated otherwise. Water diffusivity was assessed by fitting the uptake data of SHCPs at 30% RH and 25 °C to Fick's law of diffusion using the instrument software.

Water desorption experiments were performed on a Discovery TGA (TA instruments). Samples were conditioned at ~45% RH and 20 °C for 24 h to achieve water loading. Subsequently, around 20 mg of conditioned sample was transferred to the TGA and held at a constant temperature of either 30, 45, 60, 75, or 90 °C for 1 h under dry air flow (25 $mL \cdot min^{-1}$) and monitored gravimetrically.

Section 2

Heteroatom-containing HCPs

2.1. Synthesis of hypercrosslinked polymers

The linker, 4,4′-bis(chloromethyl)-1,1′-biphenyl (0.502 g, 2 mmol) and the monomer, either fluorene (0.166, 1 mmol), carbazole (0.167, 1 mmol), dibenzofuran (0.168, 1 mmol), dibenzothiophene (0.184, 1 mmol), or dibenzothiophenone sulfone (0.216 g, 1 mmol) were dissolved in 1,2-dichloroethane (5 mL) at room temperature over stirring. Upon complete dissolution of $FeCl_3$ (0,811 g, 5 mmol), the reaction mixture was heated at 80 °C overnight. The resulting solid was filtered off in a Büchner funnel and washed with methanol until the filtrate no longer ran yellow. The solid was then washed in a Soxhlet apparatus with methanol for 24 h. Excess methanol was removed by allowing the polymer to air-dry at room temperature in a fume hood for a few hours, followed by vacuum drying in an oven at 80 °C overnight. The dried network was then gently ground using a pestle and mortar, yielding fine powders (yields provided in Table S1, pictures provided in Figure S1)

Table S1. Yields of non-sulfonated heteroatom-containing HCPs

	Monomer	Yield (g)	Yield (%)
HCP-C	Fluorene	0.514	98
HCP-N	Carbazole	0.475	91
HCP-O	Dibenzofuran	0.492	94
HCP-S	Dibenzothiophene	0.522	97
HCP-SO	Dibenzothiophene sulfone	0.418	73

Figure S1. Photographs of non-sulfonated heteroatom-containing HCPs

2.2. Hypercrosslinked polymer characterisation

The formation of HCPs was confirmed using FTIR (Figure S2a). All samples exhibited characteristic aliphatic and aromatic C−H stretching bands at 3020 and 2900 cm^{-1}, respectively, as well as bands ascribed to aromatic network vibrations in the 2000–1650 cm^{-1} region. Crosslinking was confirmed by signals at 1464 cm^{-1}, indicative of newly formed methylene bridges, while a band at 798 cm^{-1} was attributed to residual C−Cl bonds. Heteroatom incorporation was verified by distinct vibrational modes characteristic of each monomer. HCP−N displayed secondary amine N−H stretching at 3443 cm^{-1} and aromatic C−N stretching at 1314 cm^{-1}. In HCP-O, a prominent feature at 1197 cm^{-1} confirmed the presence of C−O from the aryl ether. The incorporation of S was confirmed by C−S stretching bands at 570 cm^{-1} in both HCP−S and HCP−SO, while signals at 1318 and 1159 cm^{-1}, seen only in HCP-SO, were attributed to asymmetric and symmetric S=O stretching vibrations of the sulfone, respectively.

Solid-state ^{13}C cross-polarisation/magic angle spinning solid-state NMR (CP/MAS ssNMR) spectra revealed signals at ~38 ppm in all samples (Figure S2b), corresponding to newly formed methylene bridges, while a weak shoulder at ~42 ppm was attributed to unreacted C–Cl. Characteristic peaks at ~128 and ~138 ppm were observed across all HCPs, assigned to aromatic carbons in unsubstituted (C$_{Ar}$–H) and substituted (C$_{Ar}$–R) positions, respectively. Line broadening effects inherent to ssNMR limited the resolution of individual carbon environments, yet some additional peaks confirmed heteroatom incorporation. In HCP-N and HCP-O, a peak at

110 ppm was attributed to upfield shifted C_{Ar}–H adjacent to carbon directly bound to the heteroatom, while in HCP-O alone, a downfield shift to 155 ppm confirmed the presence of the aryl ether.[1]

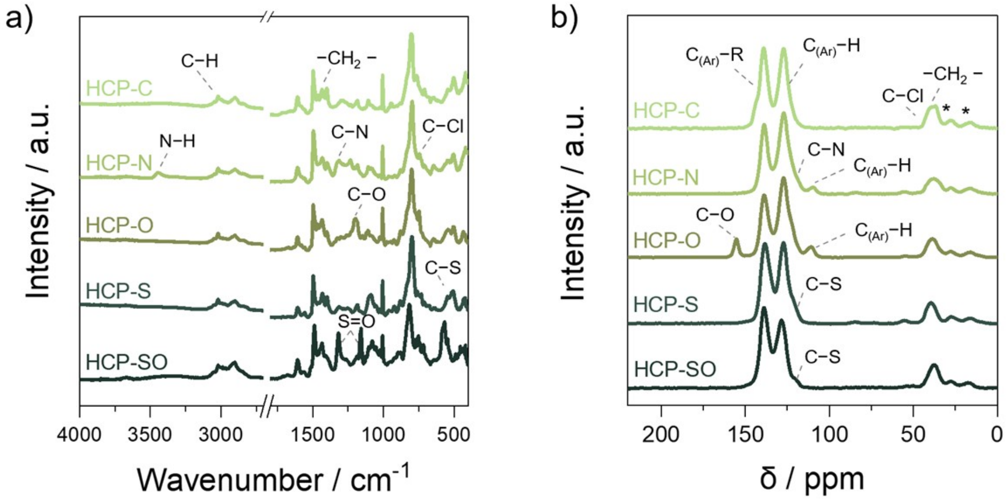

Figure S2. a) FTIR spectra and b) ^{13}C CP/MAS ssNMR spectra of heteroatom-containing HCPs

We used X-ray photoelectron spectroscopy (XPS) to confirm heteroatom incorporation at the surface of the HCP networks (Table S2). The high-resolution C 1s spectra of all samples (Figure S3-7) displayed a primary peak at a binding energy of 284.8 eV, encompassing both aromatic and aliphatic C–C bonding. Heteroatom doping led to the occurrence of an additional peak of lower intensity at 286.2 eV for C–O, 258.7 eV for C-N and 258.6 eV for C–S, respectively. A broad π–π* shake-up feature, characteristic of aromatic systems, was observed at ~291.2 eV in all cases. The high-resolution Cl 2p spectra confirmed the presence of unreacted C–Cl in all HCPs. HCP-C additionally showed some signals attributed to metal chlorides, which we assign to incomplete removal of $FeCl_3$ during washing. Element-specific high-resolution spectra also confirmed the successful incorporation of the heteroatoms into the networks (Figure S4-S7. The N 1s spectrum of HCP–N revealed a dominant feature at 400.2 eV, corresponding to C–N bonding, as well as a broad π–π* shake-up feature characteristic for aromatic amines. The presence of oxygen in HCP-O was confirmed by a peak at 533.1 eV, assigned to C−O bonding. The S 2p spectrum of HCP-S exhibited C-S peaks at 164.1 eV and 165.3 eV assigned to S $2p_{3/2}$ and $2p_{1/2}$, respectively. In contrast, HCP-SO showed a characteristic asymmetric sulfone signal comprising peaks at 168.1 eV and 169.3 eV, which corresponded to S $2p_{3/2}$ and $2p_{1/2}$.

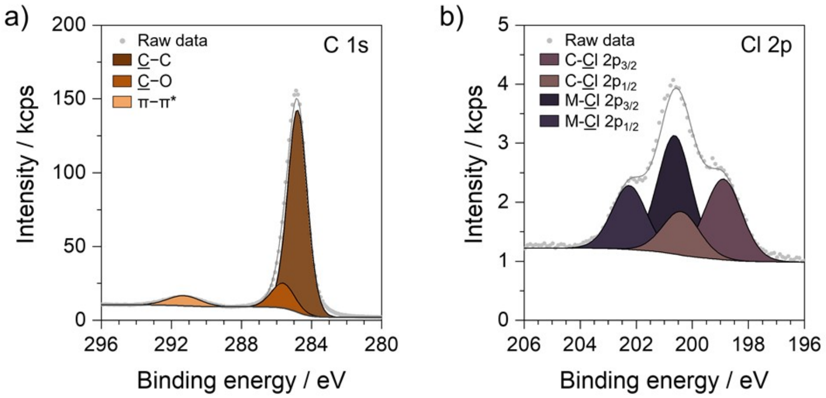

Figure S3. High-resolution X-ray photoelectron spectra of HCP-C. a) C 1s, and b) Cl 2p.

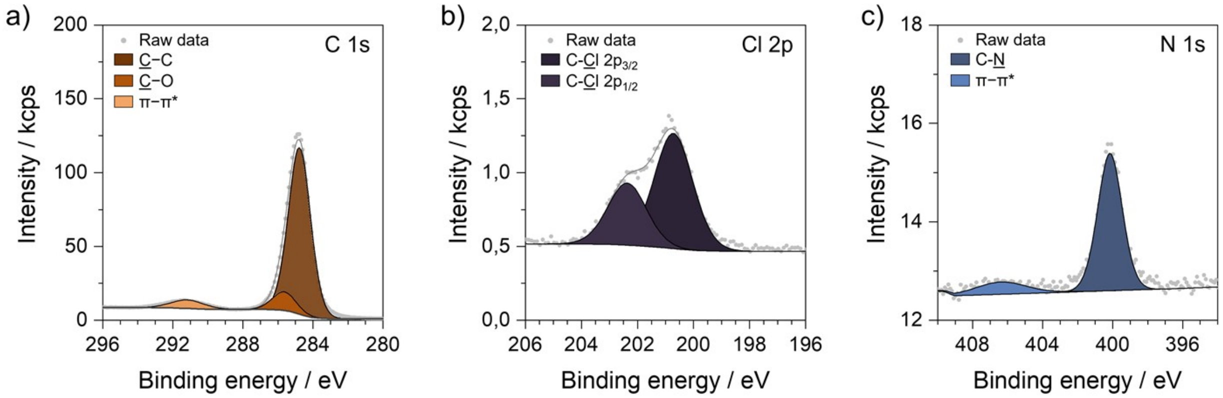

Figure S4. High-resolution X-ray photoelectron spectra of HCP-N. a) C 1s, b) Cl 2p, and c) N 1s.

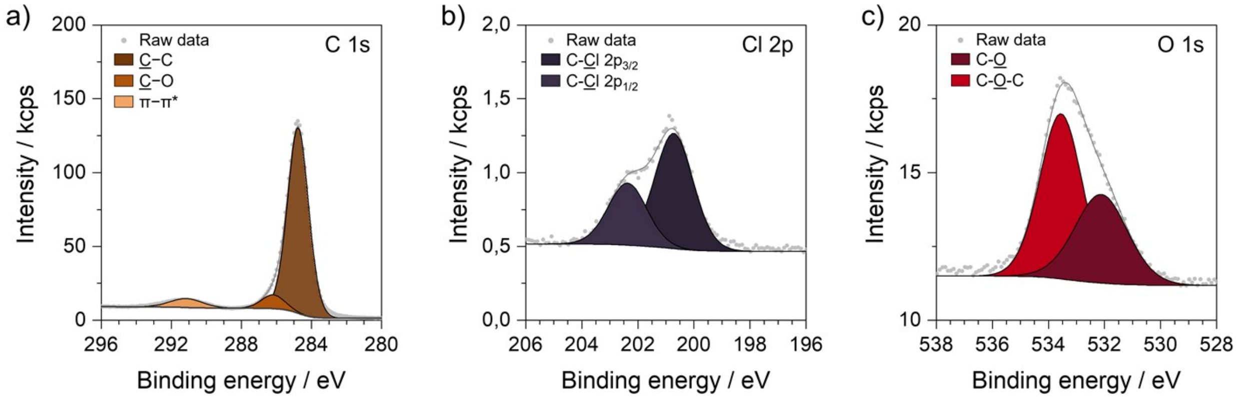

Figure S5. High-resolution X-ray photoelectron spectra of HCP-O. a) C 1s, b) Cl 2p, and c) O 1s.

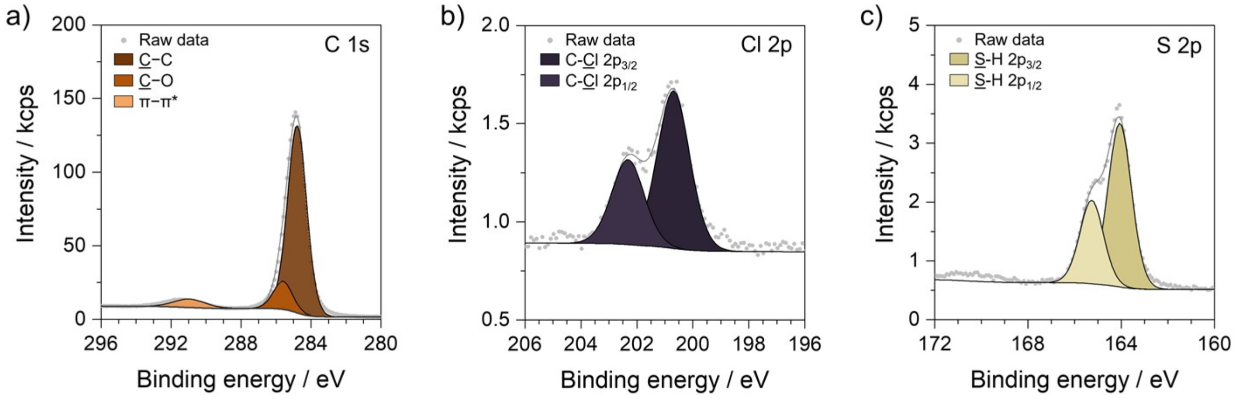

Figure S6. High-resolution X-ray photoelectron spectra of HCP-S. a) C 1s, b) Cl 2p, and c) S 2p.

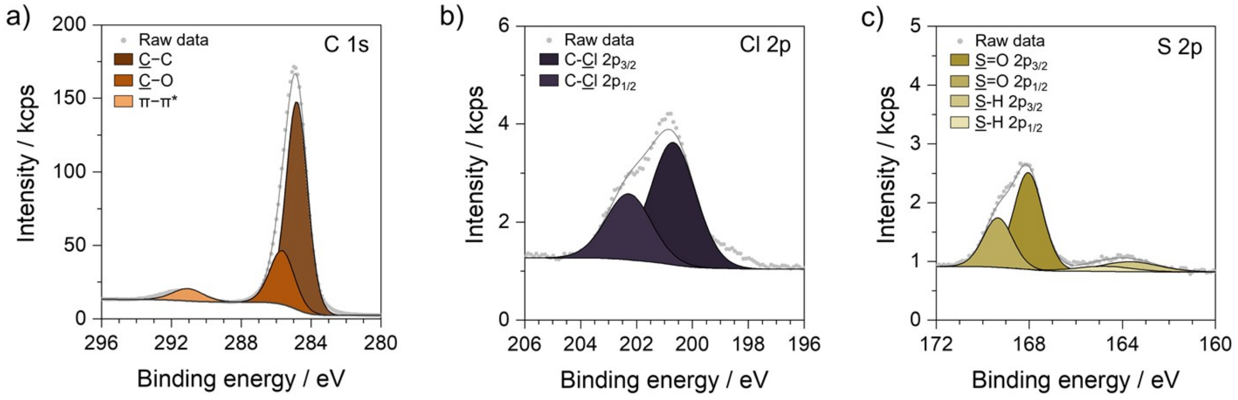

Figure S7. High-resolution X-ray photoelectron spectra of HCP-SO. a) C 1s, b) Cl 2p, and c) S 2p.

Table S2. Elemental composition of heteroatom-containing HCPs determined by XPS.

	C (wt.%)	N (wt.%)	O (wt.%)	S (wt.%)	Cl (wt.%)
HCP-C	92.87 ± 0.17	-	3.30 ± 0.25	-	3.83 ± 0.42
HCP-N	95.66 ± 0.35	1.69 ± 0.26	1.29 ± 0.30	-	1.06 ± 0.04
HCP-O	93.20 ± 0.12	-	4.28 ± 0.20	-	2.52 ± 0.08
HCP-S	93.89 ± 0.11	-	3.29 ± 0.04	3.29 ± 0.04	0.86 ± 0.04
HCP-SO	92.07 ± 0.41	-	3.36 ± 0.19	1.91 ± 0.01	2.66 ± 0.20

We performed CHNS-O elemental analysis (EA) to determine the bulk chemical composition of HCPs (Table S3) and compared it to the surface compositions determined using XPS. The results confirmed the incorporation of fluorene analogues, as reflected in the increased heteroatom content. EA also confirmed the presence of oxygen in all samples, consistent with XPS data, while residual chlorine in XPS indicated some degree of incomplete crosslinking. The discrepancies between elemental compositions from XPS and EA derive from the XPS's inability to detect hydrogen, while Cl is not determined in EA.

Table S3. Elemental composition of heteroatom-containing HCPs determined by EA.

	C (wt.%)	N (wt.%)	O (wt.%)	S (wt.%)	H (wt.%)
HCP-C	87.13 ± 0.21	-	2.03 ± 0.27	-	5.25 ± 0.03
HCP-N	88.50 ± 0.25	2.67 ± 0.02	1.12 ± 0.20	-	5.26 ± 0.02
HCP-O	89.02 ± 0.41	-	3.88 ± 0.01	-	5.06 ± 0.06
HCP-S	85.58 ± 0.19	-	1.24 ± 0.13	5.58 ± 0.06	4.91 ± 0.02
HCP-SO	88.44 ± 0.13	-	2.66 ± 0.10	1.43 ± 0.02	5.10 ± 0.01

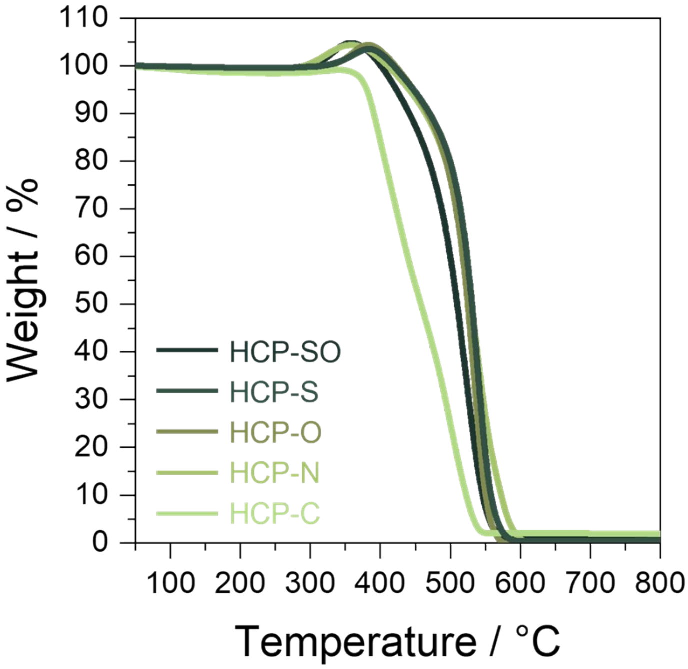

Figure S8. Thermogravimetric curves for heteroatom-containing HCPs heated up to 800 °C at a ramp rate of 10 °C·min^{-1} under air flow.

Table S4. Hansen solubility parameters (HSP) of the monomer of heteroatom-containing HCPs for Dispersion (δ_D), polarity (δ_P) and H-bonding (δ_H), LogP values, as well a total water uptake.

	Monomer	Hansen solubility parameter (MPa$^{0.5}$)			LogP	Total water uptake (g·g^{-1})
		δ_D	δ_P	δ_H		
HCP-C	Fluorene	21.9	2.8	2.8	4.2	0.07
HCP-N	Carbazole	21.4	6.0	5.4	3.7	0.14
HCP-O	Dibenzofuran	22.4	4.0	3.2	4.1	0.05
HCP-S	Dibenzothiophene	22.0	3.3	4.5	4.4	0.03
HCP-SO	Dibenzothiophene sulfone	21.1	14.4	3.4	2.4	0.29

Section 3

Sulfonated heteroatom-containing HCPs

3.1. Synthesis of sulfonated hypercrosslinked polymers

The linker, 4,4′-Bis(chloromethyl)-1,1′-biphenyl (0.502 g, 2 mmol) and the monomer, either fluorene (0.166, 1 mmol), carbazole (0.167, 1 mmol), dibenzofuran (0.168, 1 mmol), dibenzothiophene (0.184, 1 mmol), or dibenzothiophenone sulfone (0.216 g, 1 mmol) were dissolved in 1,2-dichloroethane (5 mL) at room temperature over stirring. Upon complete dissolution, a mixture of chlorosulfonic acid (0.932 g, 8 mmol) in 1,2-dichloroethane (1 mL) was added, resulting in the immediate formation of the polymer, which was further heated at 80 °C overnight. The resulting brown/black solid was washed with 50 mL of methanol in a Büchner Funnel before being washed overnight via Soxhlet extraction, again with methanol. Excess methanol was removed by allowing the polymer to air-dry at room temperature in a fume hood for a few hours, followed by vacuum drying in an oven at 80 °C overnight. The dried network was then gently ground using a pestle and mortar, yielding the final product as a fine powder (yields provided in Table S5, pictures provided in Figure S9)

Table S5. Yields of heteroatom-containing SHCPs. Percent yields are calculated based solely on the amounts of the organic precursors employed and do not consider sulfonation.

	Monomer	Yield (g)	Yield (%)
SHCP-C	Fluorene	0.777	149
SHCP-N	Carbazole	0.668	128
SHCP-O	Dibenzofuran	0.684	131
SHCP-S	Dibenzothiophene	0.763	141
SHCP-SO	Dibenzothiophene sulfone	0.734	128

Figure S9. Photographs of heteroatom-containing SHCPs

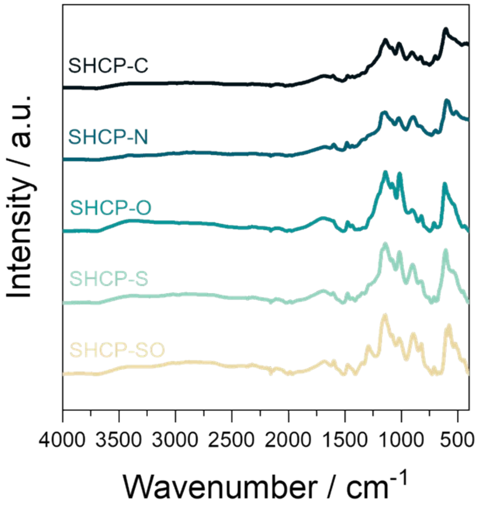

Figure S10. FTIR spectra of heteroatom-containing SHCPs.

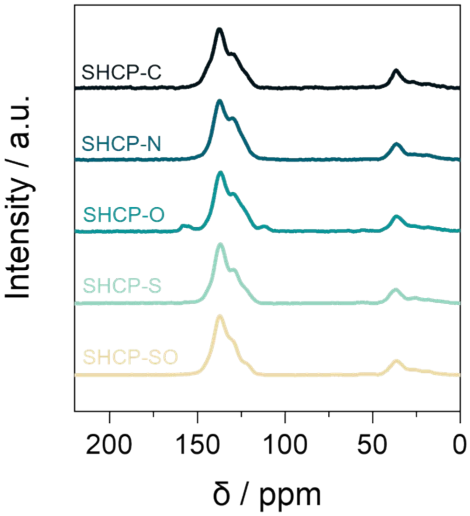

Figure S11. ^{13}C CP/MAS ssNMR spectra of heteroatom-containing SHCPs

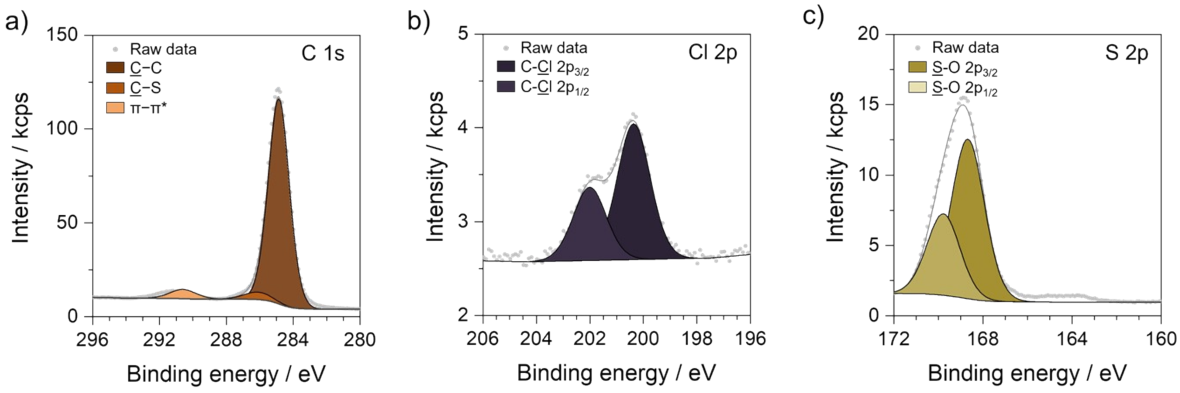

Figure S12. High-resolution X-ray photoelectron spectra of SHCP-C. a) C 1s, b) Cl 2p, and c) S 2p.

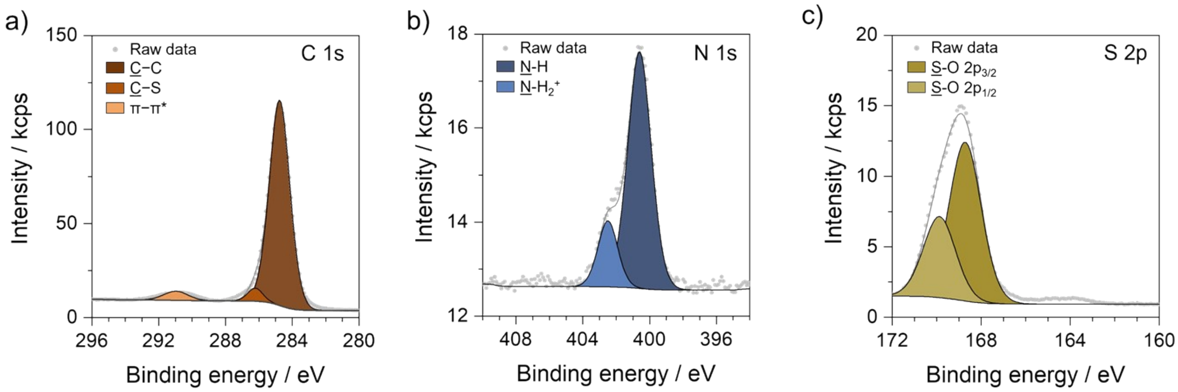

Figure S13. High-resolution X-ray photoelectron spectra of SHCP-N. a) C 1s, b) N 1s, and c) S 2p.

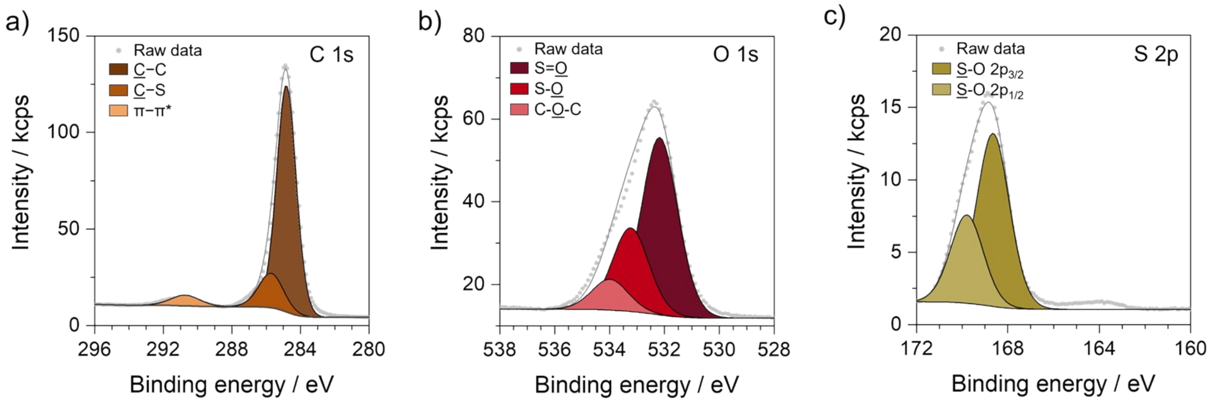

Figure S14. High-resolution X-ray photoelectron spectra of SHCP-O. a) C 1s, b) O 1s, and c) S 2p.

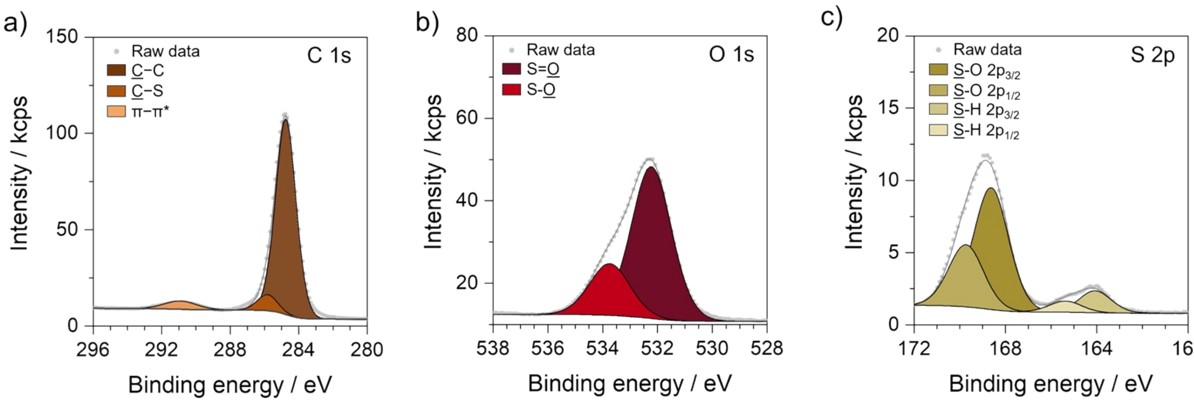

Figure S15. High resolution X-ray photoelectron spectra of SHCP-S. a) C 1s, b) Cl 2p, and c) S 2p.

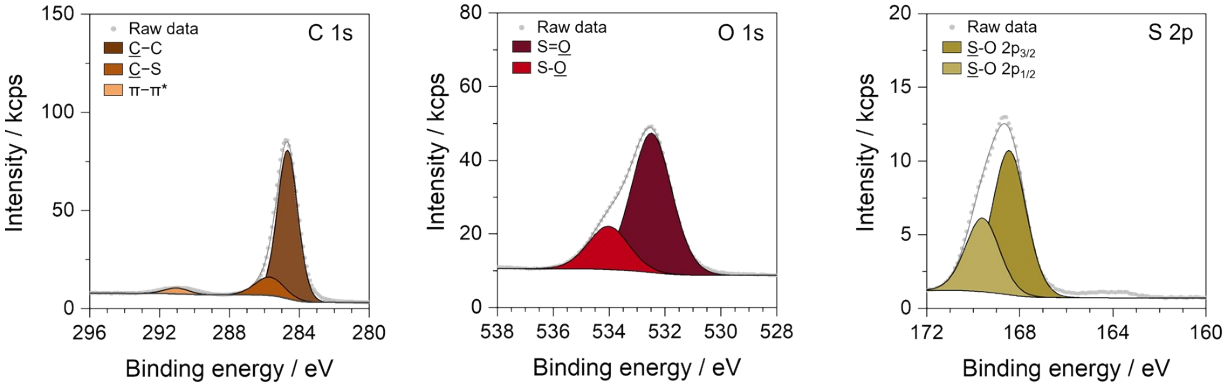

Figure S16. High-resolution X-ray photoelectron spectra of SHCP-SO. a) C 1s,b) Cl 2p, and c) S 2p.

Table S6. Elemental composition of heteroatom-containing SHCPs compared to non-sulfonated heteroatom-containing HCPs determined by XPS.

	C (wt.%)	N (wt.%)	O (wt.%)	Cl (wt.%)	S (wt.%)	S (mmol·g^{-1})
SHCP-C	62.94 ± 0.06	-	21.95 ± 0.01	0.73 ± 0.02	14.36 ± 0.03	4.47 ± 0.02
SHCP-N	61.24 ± 0.03	2.70 ± 0.12	21.40 ± 0.08	0.69 ± 0.01	13.99 ± 0.07	4.36 ± 0.02
SHCP-O	63.83 ± 0.72	-	20.81 ± 0.12	1.82 ± 0.70	13.55 ± 0.14	4.23 ± 0.04
SHCP-S	65.41 ± 1.18	-	18.50 ± 0.25	2.04 ± 0.98	14.06 ± 0.45	4.38 ± 0.14
SHCP-SO	61.05 ± 0.45	-	21.70 ± 0.25	1.05 ± 0.12	16.21 ± 0.33	5.05 ± 0.10
HCP-C	92.87 ± 0.17	-	3.30 ± 0.25	3.83 ± 0.42	-	-
HCP-N	95.66 ± 0.35	1.69 ± 0.26	1.29 ± 0.30	1.06 ± 0.04	-	-
HCP-O	93.20 ± 0.12	-	4.28 ± 0.20	2.52 ± 0.08	-	-
HCP-S	93.89 ± 0.11	-	3.29 ± 0.04	0.86 ± 0.04	3.29 ± 0.04	1.02 ± 0.01
HCP-SO	92.07 ± 0.41	-	3.36 ± 0.19	2.66 ± 0.20	1.91 ± 0.01	0.60 ± 0.01

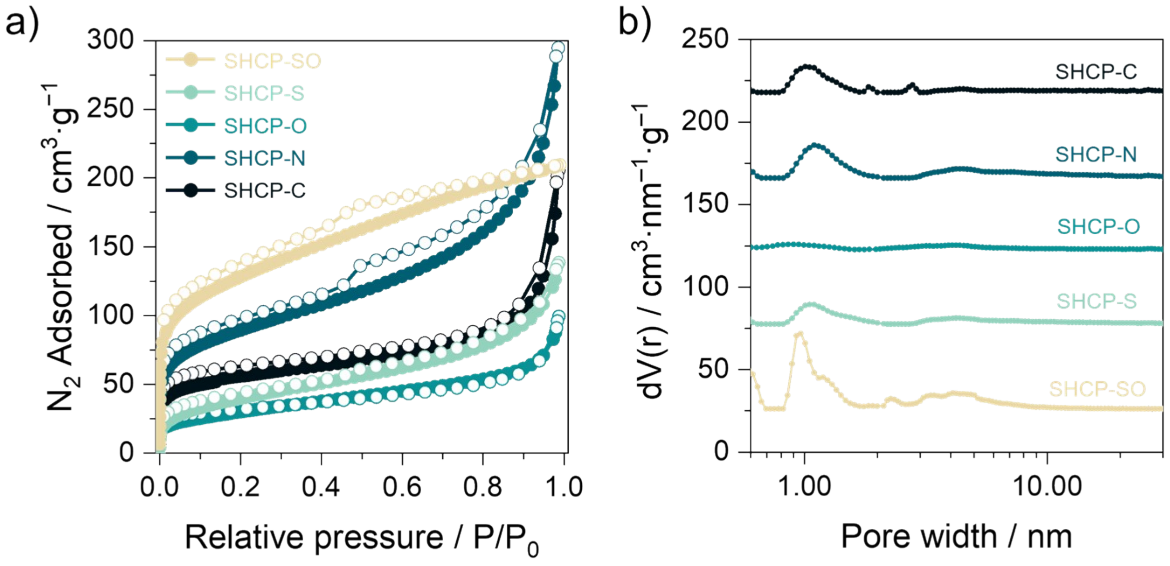

Figure S17. a) N_2 isotherms measured at −196 °C, and b) QSDFT pore size distribution of heteroatom-containing SHCPs.

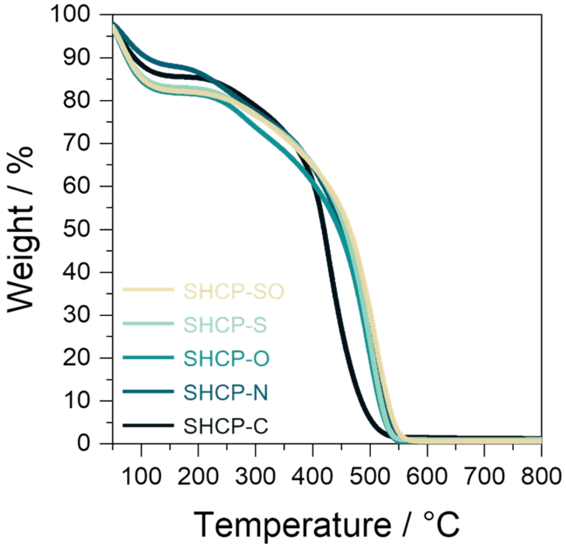

Figure S18. Thermogravimetric curves of heteroatom-containing SHCPs heated up to 800 °C at a ramp rate of 10 °C·min^{-1} under air flow.

Table S7. Heteroatom-containing SHCPs and their sulfur content determined by XPS analysis, theoretical water uptake, and experimental water uptake at 10% RH.

	Sulfonation density ($mmol \cdot g^{-1}$)	Theoretical water uptake* ($g \cdot g^{-1}$)	Water uptake at 10% RH ($g \cdot g^{-1}$)
SHCP-C	4.47 ± 0.02	0.08	0.08
SHCP-N	4.36 ± 0.02	0.08	0.07
SHCP-O	4.23 ± 0.04	0.08	0.08
SHCP-S	4.38 ± 0.14	0.08	0.08
SHCP-SO	5.05 ± 0.10	0.09	0.09

* Assuming the binding of one water molecule per sulfonate group

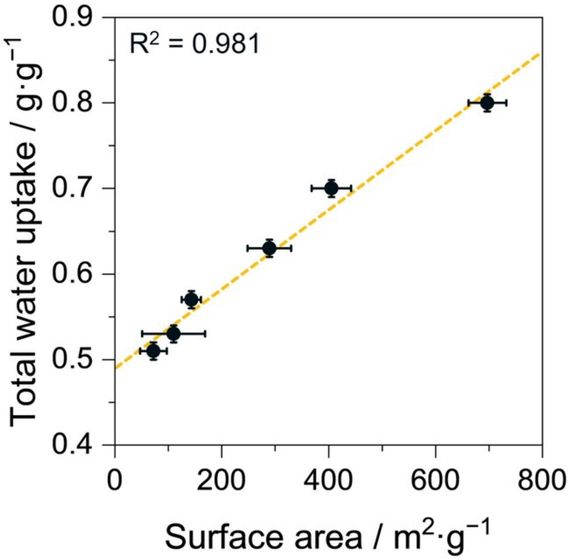

Figure S19. Linear regression fit illustrating the relationship between water uptake and surface area for SHCP-Xs and SHCP-10 from reference 10.

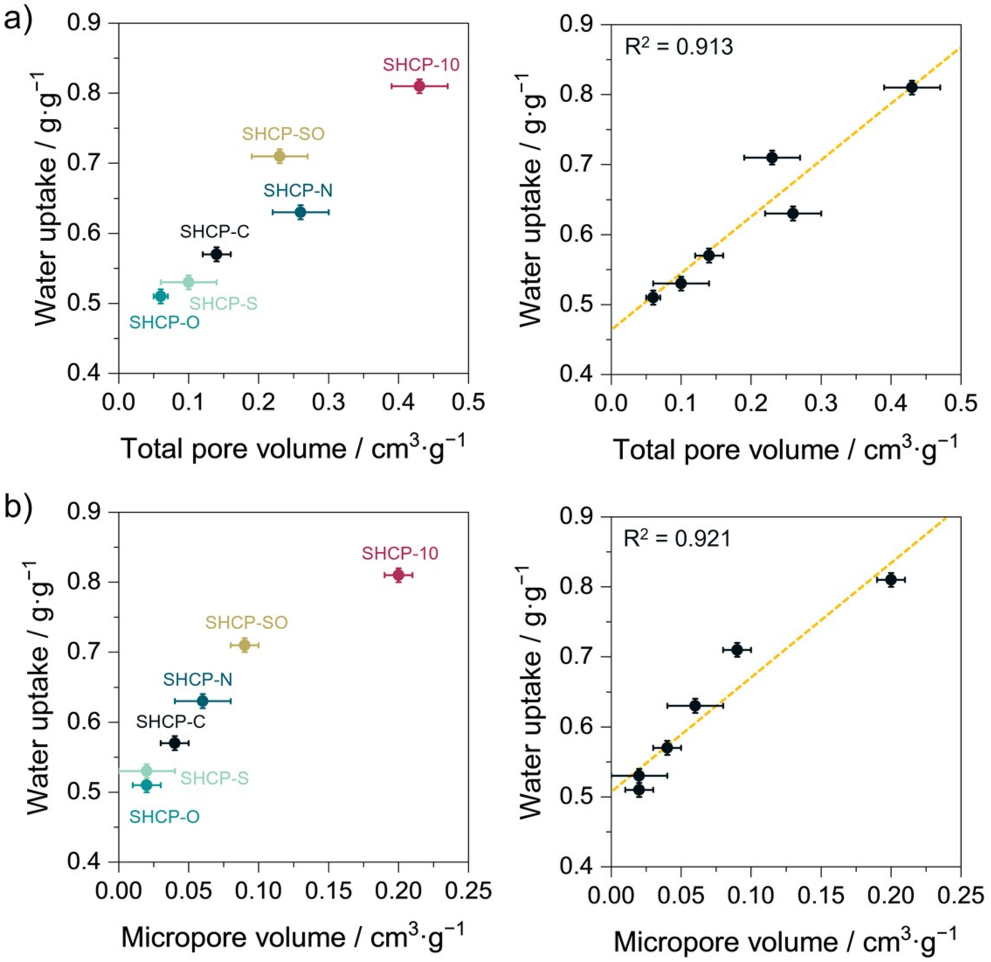

Figure S20. Water uptake plotted against a) total pore volume and b) micropore volume for SHCP-Xs and SHCP-10 from reference 10, including a linear regression fit.

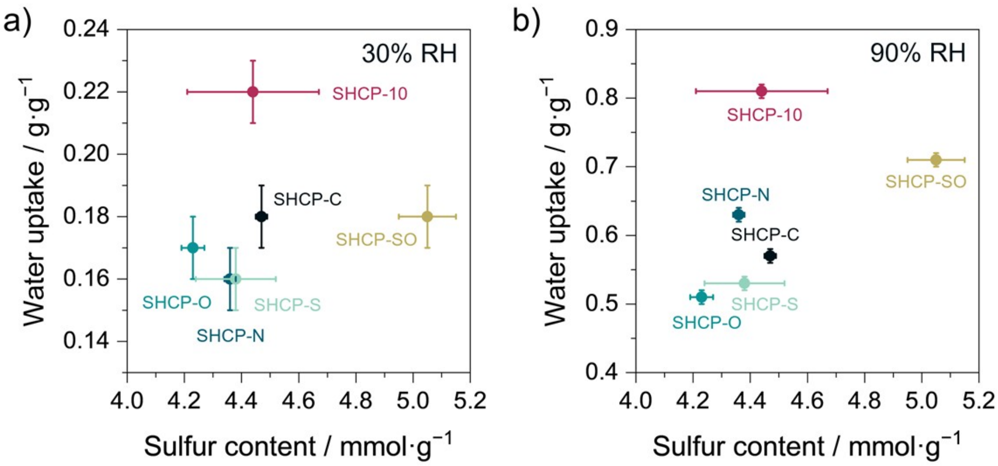

Figure S21. Water uptake at a) 30% RH and b) 90% RH plotted against sulfur content for SHCP-Xs and SHCP-10 from reference 10.

Table S8. Summary of network chemistry, BET surface area, water vapour uptake at 0.3 P/P_0 (30% RH), and total uptake capacity of various porous organic sorbents for water sorption.

Material	Network chemistry	BET surface area [m^2/g]	H_2O uptake at 0.3 P/P_0 [g/g]	Total uptake capacity [g/g]	Uptake T [°C]	Ref.
Covalent Organic Frameworks						
TpBD	Ketoenamine	341	0.02	0.15	25	2
TpBD-$(OMe)_2$	Ketoenamine / $–OCH_3$	365	0.02	0.16	25	1
TpBD-$(NO_2)_2$	Ketoenamine / $–NO_2$	90	0.02	0.09	25	1
TB-COF-Li	Ketoenamine / $–SO_3H$ / LiCl	439	0.24	0.44	25	3
COF-SO_3H	Ketoenamine / $–SO_3H$	280	0.19	0.31	25	4
SHTA-Pa	Ketoenamine / $(Enamine)_2$	1848	0.01	0.45	25	5
DHTA-Pa	$(Ketoenamine)_2$ / Enamine	2099	0.48	0.65	25	4
THTA-Pa	Ketoenamine	772	0.21	0.33	25	4
COF-ok	Ketoenamine / Pyrene	1194	0.20	0.64	25	6
Py-MPA	Imine / Pyrene	604	0.01	0.09	25	7
Py-PDCA	Imine / Pyrene / Pyridine	643	0.02	0.18	25	6
Py-HMPA	Imine / Pyrene / –OH	705	0.07	0.23	25	6
COF-432	Imine	895	0.01	0.30	25	8
3D-CageCOF-1	Imine / Phenyl ether	1040	0.16	0.30	25	9
PI-3-COF	Imine / Triazine	1340	0.03	0.46	25	10
NO-PI-3-COF	Nitrone / Triazine	664	0.15	0.24	25	9
AB-COF	Hydrazine	1209	0.33	0.44	25	11
COF-480-hydrazide	Hydrazide	989	0.32	0.44	25	10
AB-COF	Azine	1125	0.30	0.41	25	12
ATFG-COF	Keto-Enol tautomer	520	0.14	0.25	25	11
g-DZPH-COF	Vinylene / Pyridazine	960	0.39	1.00	25	13
g-DZTA-COF	Vinylene / Pyridazine / Triazine	802	0.07	0.99	25	12
DAAQ-TFP-SO3H@LiCl	Ketoenamine / $–SO_3H$ / LiCl	635	0.46	1.21	25	14
Covalent Triazine Frameworks						
bpim-CTF-400	Bis(pyridyl) imidazolium	786	0.22	0.38	25	15
bpim-CTF-500	Bis(pyridyl) imidazolium	1556	0.16	0.58	25	14
FJU-CTF-FIZ500	Benzimidazole	2042	0.21	0.82	23	16
FJU-CTF-TIZ500	Benzimidazole	1732	0.21	0.60	23	15
Amorphous micro-/mesoporous POPs						
SHCP-10	$–SO_3H$	697	0.22	0.81	25	17
2D ep-POP	Oxirane (epoxide)	852	0.10	0.41	25	18
3D ep-POP	Oxirane (epoxide)	779	0.18	0.41	25	17
OHCP-60	Thermal oxidation	462	0.06	0.35	25	19
SHCP-C	$–SO_3H$	143	0.18	0.57	25	This work
SHCP-N	N-doping / $–SO_3H$	289	0.16	0.63	25	This work
SHCP-O	O-doping / $–SO_3H$	72	0.17	0.51	25	This work
SHCP-S	S-doping / $–SO_3H$	110	0.16	0.53	25	This work
SHCP-SO	Sulfone / $–SO_3H$	405	0.18	0.71	25	This work

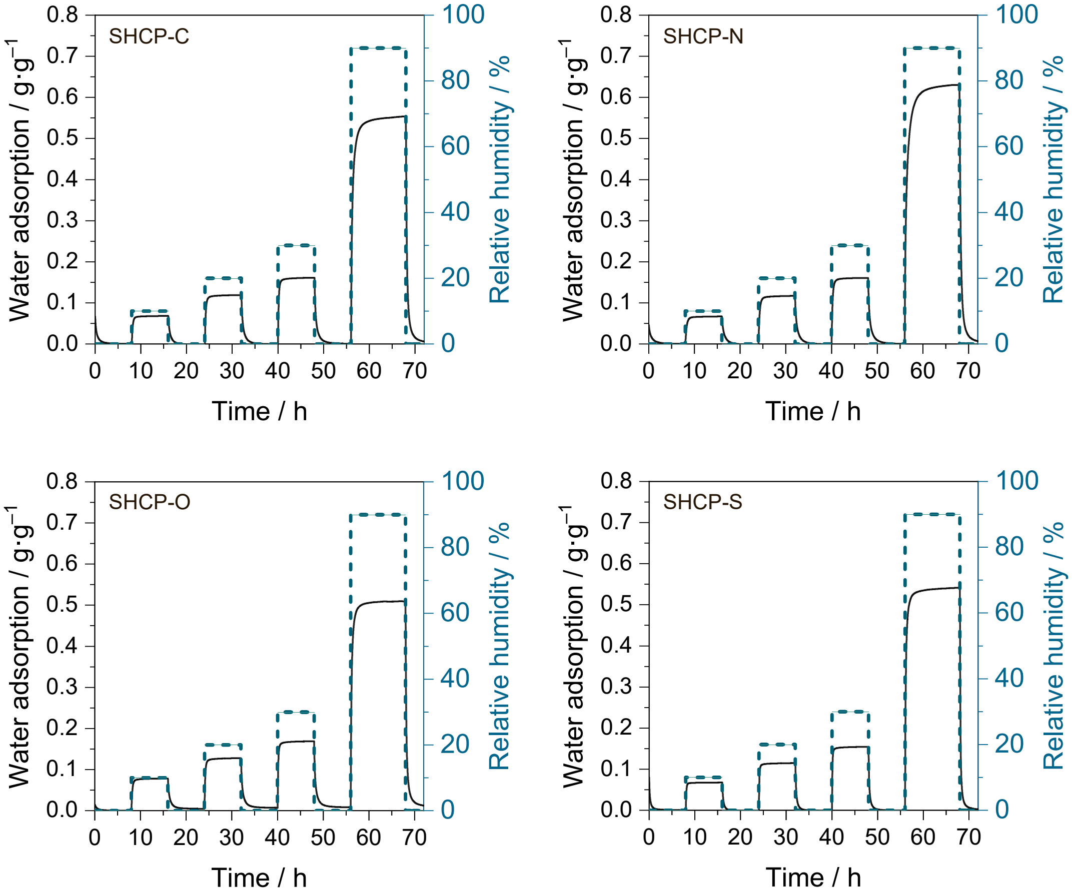

Figure S22. Dynamic vapour sorption–desorption at 10%, 20%, 30%, and 90% RH for SHCP-C, SHCP-N, SHCP-O, and SHCP-S.

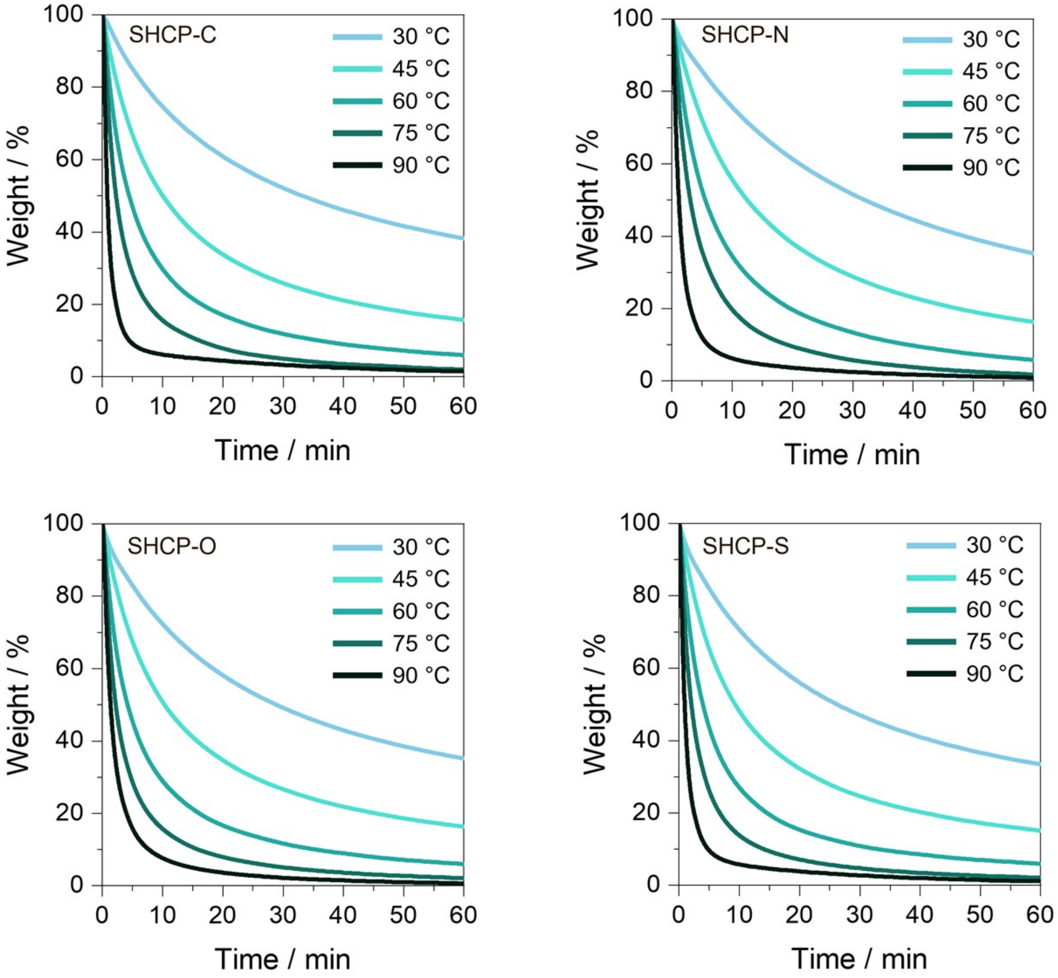

Figure S23. Water desorption from SHCP-C, SHCP-N, SHCP-O, and SHCP-S, measured using TGA. Desorption was performed at a variety of temperatures after networks were conditioned at ~45% RH and 20 °C, overnight.

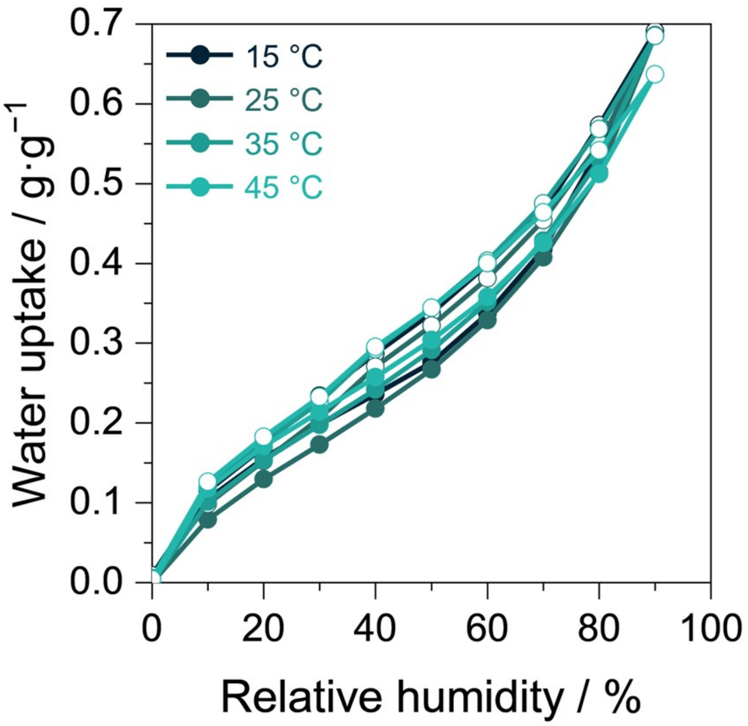

Figure S24. Water sorption-desorption isotherms of SHCP-SO recorded at 15, 25, 35, and 45 °C.

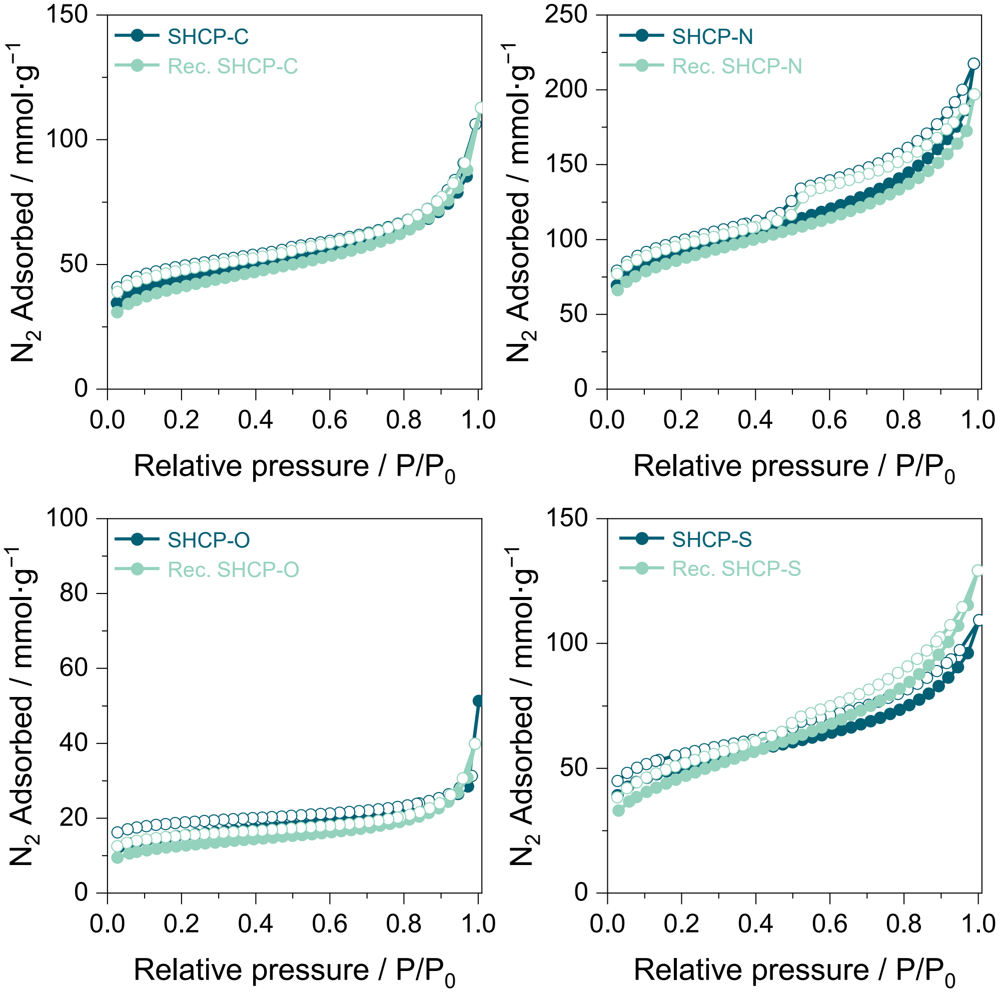

Figure S25. N_2 sorption isotherms of SHCPs before and after (rec. SHCP) heat cycling. Twenty cycles were performed, each with a 90 °C desorption step lasting 1 h.

Table S9. Summary of textural properties of SHCPs before and after (rec. SHCP) heat cycling. Twenty cycles were performed, each with a 90 °C desorption step lasting 1 h. Data includes BET specific surface area, SSA_{BET}, volume of micropores, V_{MICRO}, and total pore volume, V_{TOT} (n = 3).

Sample	SSA_{BET} ($m^2 \cdot g^{-1}$)	V_{MICRO} ($cm^3 \cdot g^{-1}$)	V_{TOT} ($cm^3 \cdot g^{-1}$)
SHCP-C	143 ± 18	0.04 ± 0.01	0.14 ± 0.02
Rec. SHCP-C	100 ± 39	0.02 ± 0.01	0.11 ± 0.04
SHCP-N	289 ± 41	0.06 ± 0.02	0.26 ± 0.04
Rec. SHCP-N	249 ± 71	0.05 ± 0.02	0.24 ± 0.02
SHCP-O	72 ± 25	0.02 ± 0.01	0.06 ± 0.01
Rec. SHCP-O	47 ± 4	0.01 ± 0.01	0.06 ± 0.01
SHCP-S	110 ± 59	0.02 ± 0.02	0.10 ± 0.04
Rec. SHCP-S	153 ± 10	0.03 ± 0.01	0.16 ± 0.02
SHCP-SO	405 ± 37	0.09 ± 0.01	0.23 ± 0.04
Rec. SHCP-SO	175 ± 17	0.05 ± 0.01	0.15 ± 0.02

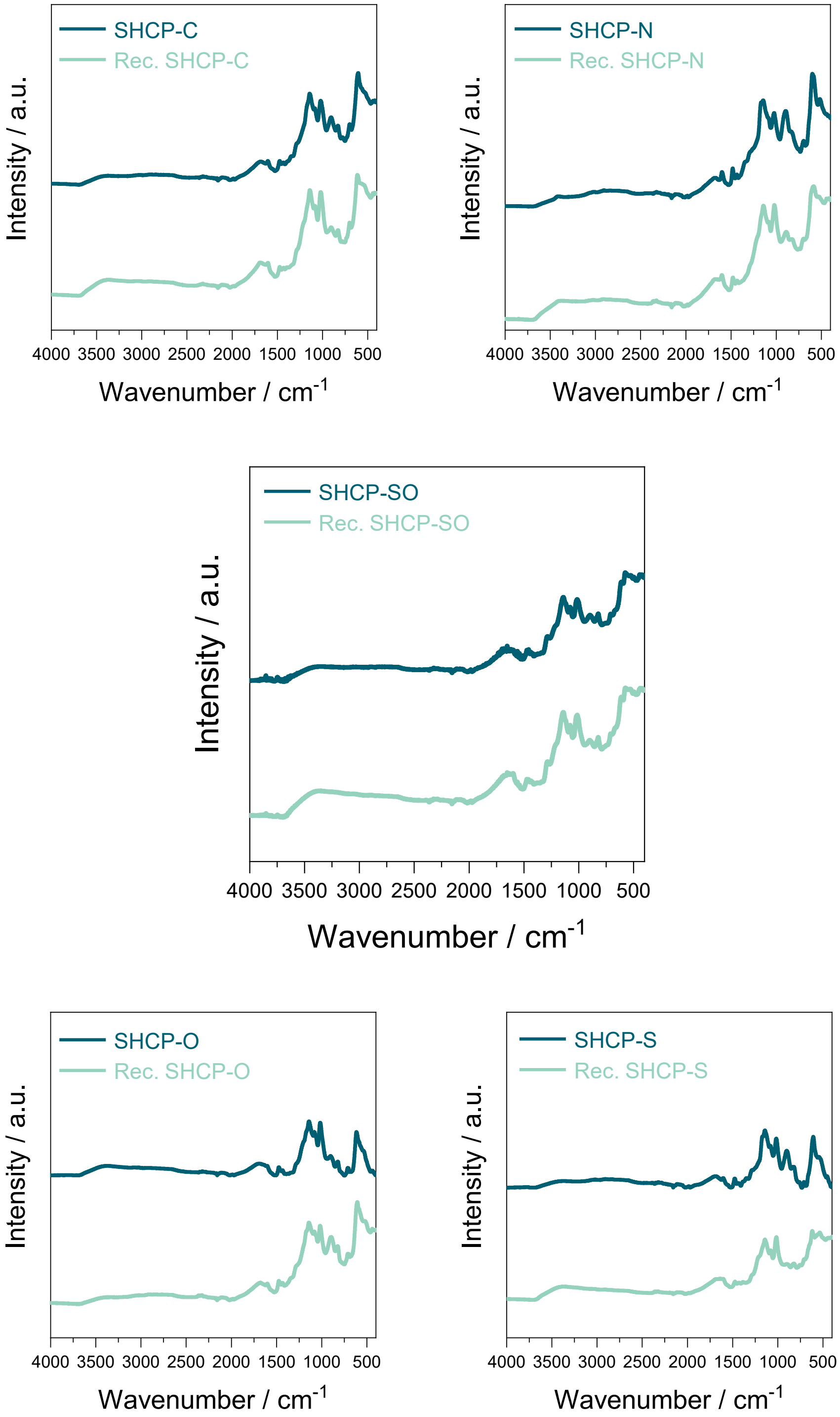

Figure S26. FTIR spectra of SHCPs before and after (rec. SHCP) heat cycling. Twenty cycles were performed, each with a 90 °C desorption step lasting 1 h.

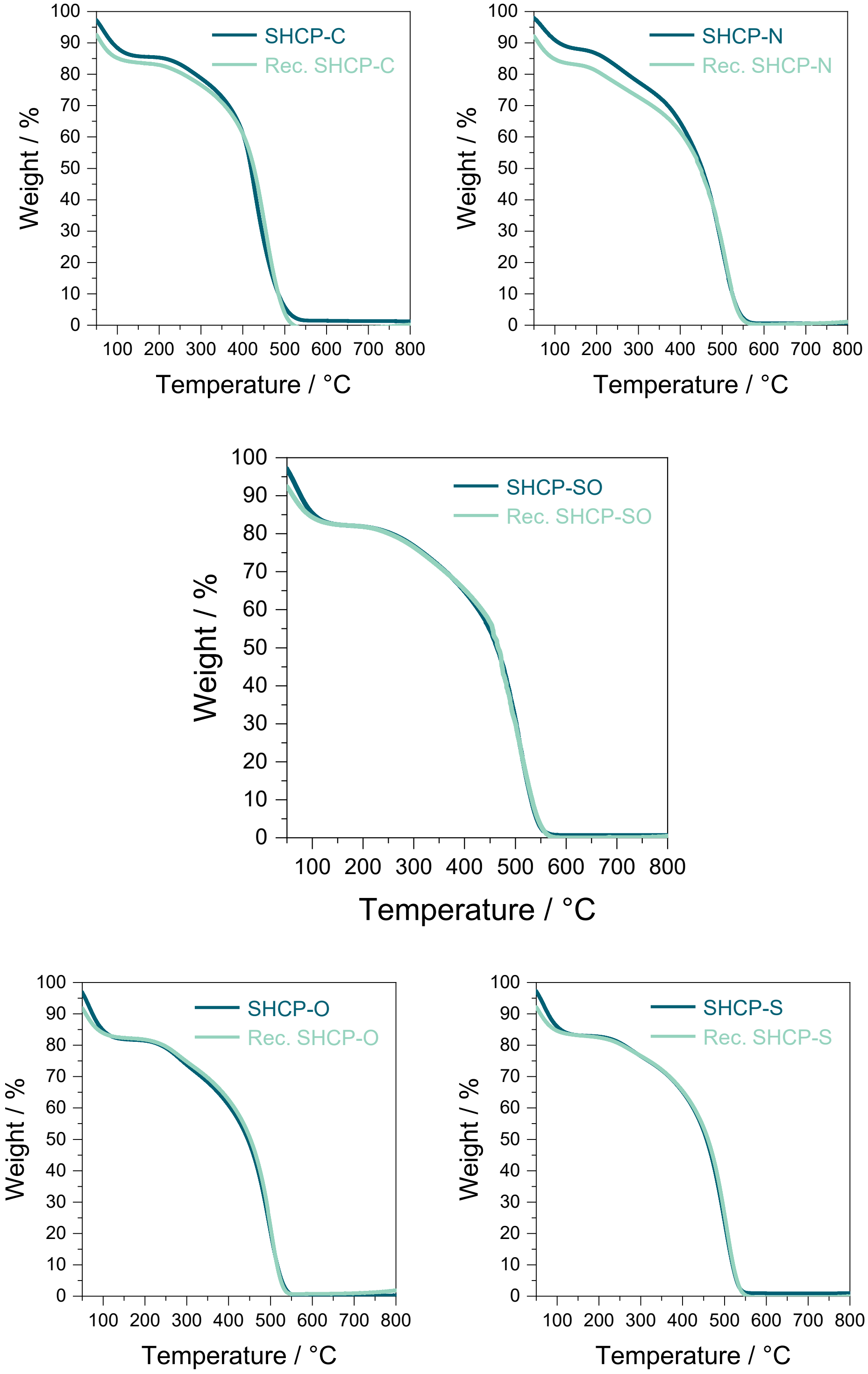

Figure S27. Thermogravimetric curves for SHCPs before and after (rec. SHCP) heat cycling. SHCPs were heated under airflow (100 mL·min^{-1}) to 800 °C at a rate of 10 °C/min.

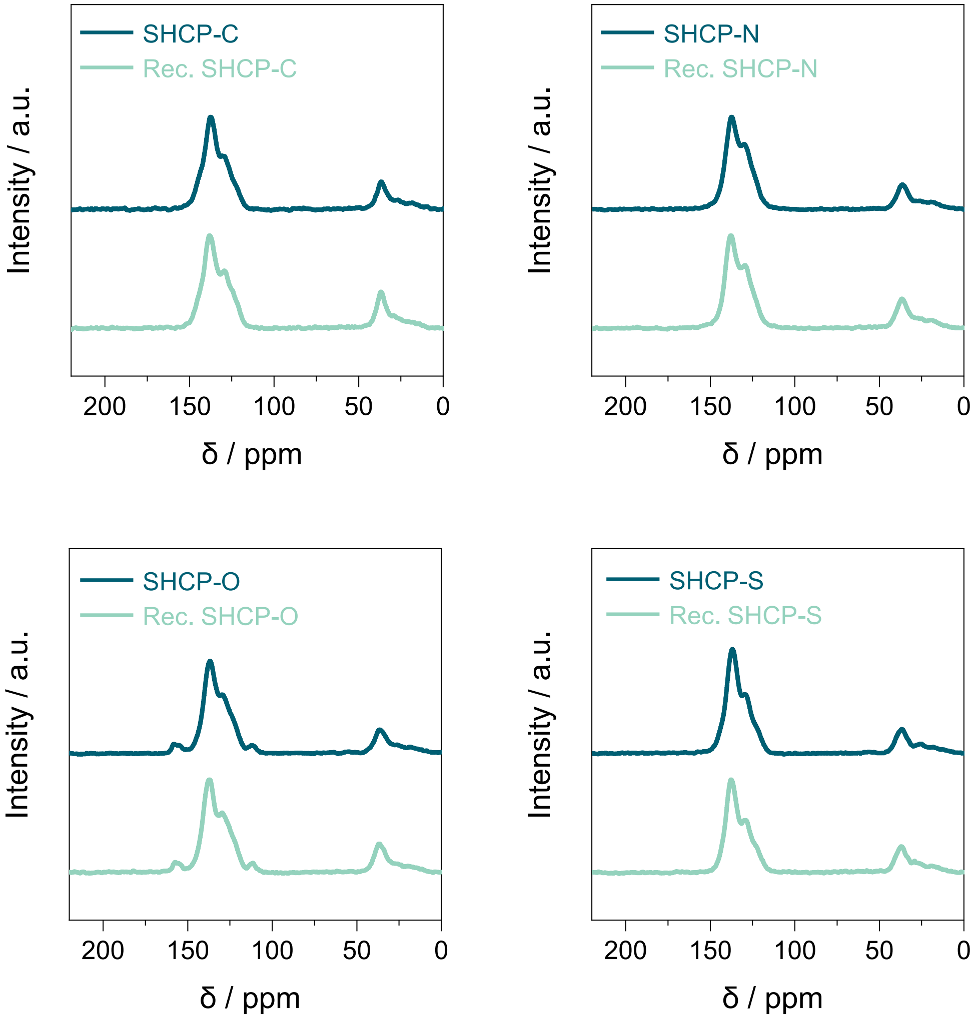

Figure S28. ^{13}C CP/MAS solid-state NMR spectra for SHCPs before and after (rec. SHCP) heat cycling.

Table S10. Elemental composition of SHCPs before and after (rec. SHCP) heat cycling determined by XPS. Twenty cycles were performed, each with a 90 °C desorption step lasting 1 h.

	C (wt.%)	N (wt.%)	O (wt.%)	Cl (wt.%)	S (wt.%)	S ($mmol \cdot g^{-1}$)
SHCP-C	62.94 ± 0.06	-	21.95 ± 0.01	0.73 ± 0.02	14.36 ± 0.03	4.47 ± 0.02
Rec. SHCP-C	62.29 ± 1.56	-	21.68 ± 0.21	1.50 ± 0.78	14.53 ± 0.57	4.53 ± 0.18
SHCP-N	61.24 ± 0.03	2.70 ± 0.12	21.40 ± 0.08	0.69 ± 0.01	13.99 ± 0.07	4.36 ± 0.02
Rec. SHCP-N	62.82 ± 0.55	1.41 ± 0.12	20.85 ± 0.01	1.02 ± 0.57	13.92 ± 0.16	4.34 ± 0.05
SHCP-O	63.83 ± 0.72	-	20.81 ± 0.12	1.82 ± 0.70	13.55 ± 0.14	4.23 ± 0.04
Rec. SHCP-O	62.58 ± 1.44	-	21.59 ± 0.02	1.69 ± 0.91	14.14 ± 0.57	4.41 ± 0.18
SHCP-S	65.41 ± 1.18	-	18.50 ± 0.25	2.04 ± 0.98	14.06 ± 0.45	4.38 ± 0.14
Rec. SHCP-S	64.40 ± 1.14		19.10 ± 0.08	1.56 ± 0.74	14.95 ± 0.50	4.66 ± 0.16
SHCP-SO	61.05 ± 0.45	-	21.70 ± 0.25	1.05 ± 0.12	16.21 ± 0.33	5.05 ± 0.10
Rec. SHCP-SO	61.42 ± 1.03		21.49 ± 0.28	0.95 ± 0.32	16.15 ± 0.43	5.04 ± 0.13

References

---

[1] Giraud, J.; Marzin, C. Comparative 13C NMR Study of Deuteriated and Undeuteriated Dibenzothiophenes, Dibenzofurans, Carbazoles, Fluorenes and Fluorenones. *Org. Magn. Reson.* **1979**, *12* (11), 647–651. https://doi.org/10.1002/mrc.1270121110.

[2] Biswal, B. P.; Kandambeth, S.; Chandra, S.; Shinde, D. B.; Bera, S.; Karak, S.; Garai, B.; Kharul, U. K.; Banerjee, R. Pore Surface Engineering in Porous, Chemically Stable Covalent Organic Frameworks for Water Adsorption. *J. Mater. Chem. A* **2015**, *3* (47), 23664–23669. https://doi.org/10.1039/C5TA07998E.

[3] Shi, Z.; Guo, Y.; Zou, X. Zhang, J.; Chen, Z.; Shan, M.; Zhang, Z.; Guo, S.; Yan, F. Low Evaporation Enthalpy Ionic Covalent Organic Frameworks for Efficient Atmospheric Water Harvesting at Low Humidity. *Angew. Chem. Int. Ed.* **2024**, accepted article, e202420619. https://doi.org/ 10.1002/anie.202420619.

[4] Schweng, P.; Li, C.; Guggenberger, P.; Kleitz, F.; Woodward, R. T. A Sulfonated Covalent Organic Framework for Atmospheric Water Harvesting. *ChemSusChem*, **2024**, *17* (20), e202301906. https://doi.org/10.1002/cssc.202301906.

[5] Sun, C.; Zhu, Y.; Shao, P.; Chen, L.; Huang, X.; Zhao, S.; Ma, D.; Jing, X.; Wang, B.; Feng, X. 2D Covalent Organic Framework for Water Harvesting with Fast Kinetics and Low Regeneration Temperature. *Angew. Chem. Int. Ed.* **2023**, *62* (11), e202217103. https://doi.org/10.1002/anie.202217103.

[6] Chen, L.-H.; Han, W.-K.; Yan, X.; Zhang, J.; Jiang, Y.; Gu, Z.-G. A Highly Stable Ortho-Ketoenamine Covalent Organic Framework with Balanced Hydrophilic and Hydrophobic Sites for Atmospheric Water Harvesting. *ChemSusChem* **2022**, *15* (24), e202201824. https://doi.org/10.1002/cssc.202201824.

[7] Liu, Y.; Han, W.-K.; Chi, W.; Fu, J.-X.; Mao, Y.; Yan, X.; Shao, J.-X.; Jiang, Y.; Gu, Z.-G. One-Dimensional Covalent Organic Frameworks with Atmospheric Water Harvesting for Photocatalytic Hydrogen Evolution from Water Vapor. *Appl. Catal. B.* **2023**, *338*, 123074. https://doi.org/10.1016/j.apcatb.2023.123074.

[8] Nguyen, H. L.; Hanikel, N.; Lyle, S. J.; Zhu, C.; Proserpio, D. M.; Yaghi, O. M. A Porous Covalent Organic Framework with Voided Square Grid Topology for Atmospheric Water Harvesting. *J. Am. Chem. Soc.* **2020**, *142* (5), 2218–2221. https://doi.org/10.1021/jacs.9b13094.

[9] Zhu, Q.; Wang, X.; Clowes, R.; Cui, P.; Chen, L.; Little, M. A.; Cooper, A. I. 3D Cage COFs: A Dynamic Three-Dimensional Covalent Organic Framework with High-Connectivity Organic Cage Nodes. *J. Am. Chem. Soc.* **2020**, *142* (39), 16842–16848. https://doi.org/10.1021/jacs.0c07732.

[10] Grunenberg, L.; Savasci, G.; Emmerling, S. T.; Heck, F.; Bette, S.; Cima Bergesch, A.; Ochsenfeld, C.; Lotsch, B. V. Postsynthetic Transformation of Imine- into Nitrone-Linked Covalent Organic Frameworks for Atmospheric Water Harvesting at Decreased Humidity. *J. Am. Chem. Soc.* **2023**, *145* (24), 13241–13248. https://doi.org/10.1021/jacs.3c02572.

[11] Nguyen, H. L.; Gropp, C.; Hanikel, N.; Möckel, A.; Lund, A.; Yaghi, O. M. Hydrazine-Hydrazide-Linked Covalent Organic Frameworks for Water Harvesting. *ACS Cent. Sci.* **2022**, *8* (7), 926–932. https://doi.org/10.1021/acscentsci.2c00398.

[12] Stegbauer, L.; Hahn, M. W.; Jentys, A.; Savasci, G.; Ochsenfeld, C.; Lercher, J. A.; Lotsch, B. V. Tunable Water and CO_2 Sorption Properties in Isostructural Azine-Based Covalent Organic Frameworks through Polarity Engineering. *Chem. Mater.* **2015**, *27* (23), 7874–7881. https://doi.org/10.1021/acs.chemmater.5b02151.

[13] Mou, K.; Meng, F.; Zhang, Z.; Li, X.; Li, M.; Jiao, Y.; Wang, Z.; Bai, X.; Zhang, F. Pyridazine-Promoted Construction of Vinylene-Linked Covalent Organic Frameworks with Exceptional Capability of Stepwise Water Harvesting. *Angew. Chem. Int. Ed.* **2024**, *63* (34), e202402446. https://doi.org/10.1002/anie.202402446.

[14] Liu, Y.; Zhu, Y.; Mao, Q.; Chen, W. Enhanced Hydrophilicity of DAAQ-TFP COFs via Sulfonate Modification for Air Water Harvesting in Arid Environment. *Small* **2024**, *20* (51), 2406803. https://doi.org/ 10.1002/smll.202406803.

[15] Park, K.; Lee, K.; Kim, H.; Ganesan, V.; Cho, K.; Jeong, S. K.; Yoon, S. Preparation of Covalent Triazine Frameworks with Imidazolium Cations Embedded in Basic Sites and Their Application for CO_2 Capture. *J. Mater. Chem. A* **2017**, *5* (18), 8576–8582. https://doi.org/10.1039/C6TA11226A.

[16] Huang, J.; Yang, Y.; Chen, L.; Zhang, Z.; Xiang, S. Atmospheric Water Harvesting in Microporous Organic Polymers Constructed from Trazine and Benzimidazole Units. *ZAAC* **2023**, *649* (19), e202300167. https://doi.org/10.1002/zaac.202300167.

[17] Schweng, P.; Mayer, F.; Galehdari, D.; Weiland, K.; Woodward, R. T. A Robust and Low-Cost Sulfonated

---

Hypercrosslinked Polymer for Atmospheric Water Harvesting. *Small* **2023**, *19* (50), 2304562. https://doi.org/10.1002/smll.202304562.

[18] Byun, Y.; Coskun, A. Epoxy-Functionalized Porous Organic Polymers via the Diels–Alder Cycloaddition Reaction for Atmospheric Water Capture. *Angew. Chem. Int. Ed.* **2018**, *57* (12), 3173–3177. https://doi.org/10.1002/anie.201800380.

[19] Schweng, P.; Präg, L.; Woodward, R. T.; Regulating the Hydrophilicity of Hyper-Cross-Linked Polymers via Thermal Oxidation for Atmospheric Water Harvesting. *ACS Appl. Mater. Interfaces* **2024**, *16* (43), 58566–58572. https://doi.org/ 10.1021/acsami.4c11013